

See discussions, stats, and author profiles for this publication at: <https://www.researchgate.net/publication/49819229>

# Infrared spectroscopy of ionized corannulene in the gas phase

ARTICLE in THE JOURNAL OF CHEMICAL PHYSICS · FEBRUARY 2011

Impact Factor: 2.95 · DOI: 10.1063/1.3540661 · Source: PubMed

CITATIONS

12

READS

23

4 AUTHORS, INCLUDING:



Héctor Alvaro Galué

10 PUBLICATIONS 50 CITATIONS

SEE PROFILE



Corey Rice

University of Basel

32 PUBLICATIONS 340 CITATIONS

SEE PROFILE



Jeffrey D. Steill

Oak Ridge National Laboratory

84 PUBLICATIONS 1,460 CITATIONS

SEE PROFILE

# Infrared spectroscopy of ionized corannulene in the gas phase

Héctor Alvaro Galué,<sup>1</sup> Corey A. Rice,<sup>2</sup> Jeffrey D. Steill,<sup>1</sup> and Jos Oomens<sup>1,3,a)</sup>

<sup>1</sup>*FOM Institute for Plasma Physics "Rijnhuizen," Edisonbaan 14, 3439MN Nieuwegein, The Netherlands*

<sup>2</sup>*Departement Chemie, Universität Basel, Klingelbergstrasse 80 CH-4056 Basel, Switzerland*

<sup>3</sup>*van 't Hoff Institute for Molecular Sciences, University of Amsterdam, Science Park 904, 1098XH Amsterdam, The Netherlands*

(Received 7 October 2010; accepted 21 December 2010; published online 3 February 2011)

The gas-phase infrared spectra of radical cationic and protonated corannulene were recorded by infrared multiple-photon dissociation (IRMPD) spectroscopy using the IR free electron laser for infrared experiments. Electrospray ionization was used to generate protonated corannulene and an IRMPD spectrum was recorded in a Fourier-transform ion cyclotron resonance mass spectrometer monitoring H-loss as a function of IR frequency. The radical cation was produced by 193-nm UV photoionization of the vapor of corannulene in a 3D quadrupole trap and IR irradiation produces H, H<sub>2</sub>, and C<sub>2</sub>H<sub>x</sub> losses. Summing the spectral response of the three fragmentation channels yields the IRMPD spectrum of the radical cation. The spectra were analyzed with the aid of quantum-chemical calculations carried out at various levels of theory. The good agreement of theoretical and experimental spectra for protonated corannulene indicates that protonation occurs on one of the peripheral C-atoms, forming an *sp*<sup>3</sup> hybridized carbon. The spectrum of the radical cation was examined taking into account distortions of the C<sub>5v</sub> geometry induced by the Jahn–Teller effect as a consequence of the degenerate <sup>2</sup>E<sub>1</sub> ground electronic state. As indicated by the calculations, the five equivalent C<sub>s</sub> minima are separated by marginal barriers, giving rise to a dynamically distorted system. Although in general the character of the various computed vibrational bands appears to be in order, only a qualitative match to the experimental spectrum is found. Along with a general redshift of the calculated frequencies, the IR intensities of modes in the 1000–1250 cm<sup>−1</sup> region show the largest discrepancy with the harmonic predictions. In addition to CH “in-plane” bending vibrations, these modes also exhibit substantial deformation of the pentagonal inner ring, which may relate directly to the vibronic interaction in the radical cation. © 2011 American Institute of Physics. [doi:10.1063/1.3540661]

## I. INTRODUCTION

Corannulene (C<sub>20</sub>H<sub>10</sub>) is a highly symmetric molecule (C<sub>5v</sub>) belonging to the family of polycyclic aromatic hydrocarbons (PAHs) composed of five perifused aromatic rings around a central five-membered ring. The molecular structure resembles that of coronene (C<sub>24</sub>H<sub>12</sub>), which consists of six aromatic rings symmetrically arranged around an inner six-membered ring and which possesses D<sub>6h</sub> symmetry. As shown by x-ray diffraction,<sup>1</sup> the bonds between the carbon atoms of the pentagonal ring and the peripheral benzenic rings are significantly out of the plane in corannulene. Therefore, the adopted curved geometry reduces the aromatic character of corannulene as compared to planar coronene.

Being the smallest stable PAH adopting a bowl-shaped structure, corannulene resembles a fragment of a fullerene (C<sub>60</sub>) with the outer-perimeter carbons terminated by hydrogen atoms. Corannulene has been suggested to possess structural and electronic properties relevant to superconductivity.<sup>2</sup> Encapsulation of smaller molecules in the bowl-shaped geometry has turned attention to possible applications in hydrogen storage<sup>3</sup> and molecular recognition<sup>4</sup> with corannulene pincers. Moreover, the occurrence of corannulene in interstellar environments has been suggested and possibly plays a role

in the formation of interstellar C<sub>60</sub>.<sup>5</sup> Owing to its large permanent dipole moment<sup>6</sup> of around 2.1 D, corannulene has been the target of several laboratory and observational microwave studies.<sup>7</sup> As compared to planar regular PAHs, corannulene offers an opportunity to detect an individual PAH molecule in space based on its microwave spectrum.

Density functional theory (DFT) methods have been extensively applied to planar PAH systems<sup>8</sup> and they have proven to yield calculated harmonic IR frequencies which are in good agreement with experimental IR vibrational spectra, both for neutral and radical cation forms<sup>9,10</sup> as well as for positively charged PAH derivatives.<sup>11,12</sup> These methods have also been applied to PAHs containing a five-membered ring,<sup>13</sup> but the performance of these methods for nonplanar corannulene in its cationic state has not been verified against experimental data.

Neutral corannulene has a fivefold symmetry axis and the highest occupied molecular orbital (HOMO) is degenerate. Upon removal of an electron, the ion becomes energetically unstable and is subject to Jahn–Teller (JT) distortion.<sup>14</sup> This poses substantial challenges to characterizations of the radical species by quantum-chemical methods. Here we present the first gas-phase IR spectrum of the corannulene radical cation, which is compared directly to spectra predicted using different computational approaches.

Gas-phase IR spectra of two singly positively charged forms of corannulene, protonated and radical cation, were

<sup>a)</sup>Author to whom correspondence should be addressed. Electronic mail: joso@rijnhuizen.nl.

investigated. Interestingly, the former has a closed shell electronic structure ( $^1A$ ) and lowered symmetry, while the latter has an open shell electronic structure ( $^2E_1$ ) and undergoes JT distortion. This difference is clearly observable in their spectra. Spectra were measured via resonant IR multiple-photon dissociation (IRMPD) and characterized using standard DFT calculations at various levels of theory. For comparison, the IR spectrum of neutral corannulene ( $^1A_1$ ) was also measured and changes in the IR activity as a consequence of protonation and ionization are discussed. For the radical cation, the effects of destabilization of the degenerate  $^2E_1$ -state are rationalized and two optimized JT-distorted  $C_s$  geometries are determined in order to calculate their vibrational spectra. Finally, to gain further insights into the experimental IR spectrum of cationic corannulene, we compare the IR spectra of the coronene and corannulene radical cations.

## II. METHODS

### A. Experimental

Corannulene was synthesized via solution-phase chemistry by the Siegel group.<sup>15</sup> The fine dust particles that resulted from the procedure were used without further preparation.

The apparatus employed to record the IRMPD spectrum of the corannulene radical cation was described in detail previously,<sup>16</sup> and has been successfully used to record the IRMPD spectra of other PAHs with sizes ranging from naphthalene up to coronene<sup>10</sup> as well as some derivatives.<sup>11</sup> Briefly, the radical cation of corannulene was created by evaporating the solid sample from an effusive source heated to  $\sim 353$  K. The neutral vapor was photoionized by the absorption of two 193-nm (6.4 eV) photons of an ArF laser focused into the center of a quadrupole ion trap. The ionization potential of corannulene is 7.2 eV (Ref. 17) and the excess energy induces some dissociation. Shortly after the UV pulse, the RF amplitude was briefly (2 ms) ramped up, axially ejecting the photodissociation fragments from the trap thus isolating the precursor corannulene cation. The isolated ions are then spectroscopically interrogated with the high-power IR radiation of the free electron laser for infrared experiments, FELIX.<sup>18</sup> Each FELIX macropulse of around 60 mJ in energy is composed of  $\sim 5000$  micropulses. Multiple IR photons are sequentially absorbed whenever the laser is in resonance with a vibrational transition of the cation, leading to a population of highly vibrationally excited cations that decay via dissociation. The parent and fragment ions are detected with a linear time of flight mass spectrometer attached to the ion trap. An IRMPD spectrum is then recorded by monitoring the fragmentation yield ( $H$ ,  $H_2$ , and  $C_2H_x$  loss) as a function of the IR frequency of the laser.

The IRMPD spectrum of protonated corannulene was obtained using a Fourier-transform ion cyclotron resonance mass spectrometer (FTICR-MS) also coupled to the IR beamline of FELIX.<sup>19</sup> Protonated corannulene cations were produced by electrospray ionization (ESI), and for this purpose, corannulene was dissolved in methanol with a small amount of ammonium acetate added, as was previously used for several PAH species.<sup>20</sup> Ions were accumulated in a hexapole trap

prior to injection into the ion cyclotron resonance cell, where the ions were mass-isolated and subsequently irradiated for 7 s at each IR frequency. The only observed fragmentation channel was atomic hydrogen loss. An IRMPD spectrum was obtained by monitoring the resulting dissociation yield as a function of wavelength of FELIX.

### B. Theoretical

Optimized ground-state geometries were generated for the radical cation and protonated corannulene using several *ab initio*<sup>21</sup> and DFT levels of theory. These include the spin-restricted open-shell Hartree–Fock (ROHF),<sup>22</sup> the Becke electron-exchange<sup>23</sup> with Perdew,<sup>24</sup> or Lee *et al.*<sup>25</sup> gradient-corrected local density approximation correlation pure functionals: B-P86 and B-LYP; and the three-parameter hybrid functionals: B3-P86 and B3-LYP.<sup>26</sup> The basis-set functions employed range from double- to triple- $\zeta$  split-valence sets of Pople and the correlation-consistent polarized valence double- $\zeta$  (cc-pVDZ) set of Dunning.<sup>27</sup> For Pople basis sets, *d* and *p* polarization functions for C and H atoms were used, respectively. All calculations were performed using the GAUSSIAN 03 suite of programs.<sup>28</sup> At each level of theory employed, vibrational modes were computed by solving the Hessian as implemented in GAUSSIAN 03. The frequencies (i.e., Hessian eigenvalues) of the modes were convoluted with a 30  $\text{cm}^{-1}$  FWHM Gaussian line-shape function to generate synthetic IR spectra.

In addition to the cations, the  $C_{5v}$ -symmetry structure of neutral corannulene was investigated at the BP86/6-311G(d,p) and B3LYP/6-311G(p,d) levels, and used as a structural reference for spectral characterization of the cationic systems. Frequencies were convoluted with a 5  $\text{cm}^{-1}$  FWHM Gaussian function to simulate the experimental FTIR spectrum of corannulene recorded in a KBr pellet.

For protonated corannulene, the  $C_1$ -optimized geometry and the Hessian matrix were also computed at BP86/6-311G(d,p) and B3LYP/6-311G(d,p) levels. The calculated PES of the  $^1A$  state has a well-defined global minimum located at the  $C_1$  point, and the computed vibrational modes at this point produce no imaginary frequencies and, moreover, reproduce the experimental IRMPD spectrum reasonably well (*vide infra*). For the corannulene radical cation,  $C_{5v}$ -geometry optimizations at BP86, B3LYP, and other levels of theory were performed, but did not converge to a stable structure because the  $C_{5v}$  symmetry point on the degenerate  $^2E_1$ -state PES is located at a JT conical intersection. JT distortion lifts the degeneracy of the electronic states and produces a lowest energy structure at a lower symmetry geometry.<sup>14</sup> Symmetry considerations within the JT theorem are borne in mind to find optimized JT-distorted geometries associated with the two electronic states that form the conical intersection. JT-distorted geometries and fundamental frequencies were computed using the four methods mentioned above, and for each one of them, basis sets of different sizes were employed. The results of these computations are evaluated against the experimental IRMPD spectrum of the corannulene radical cation.

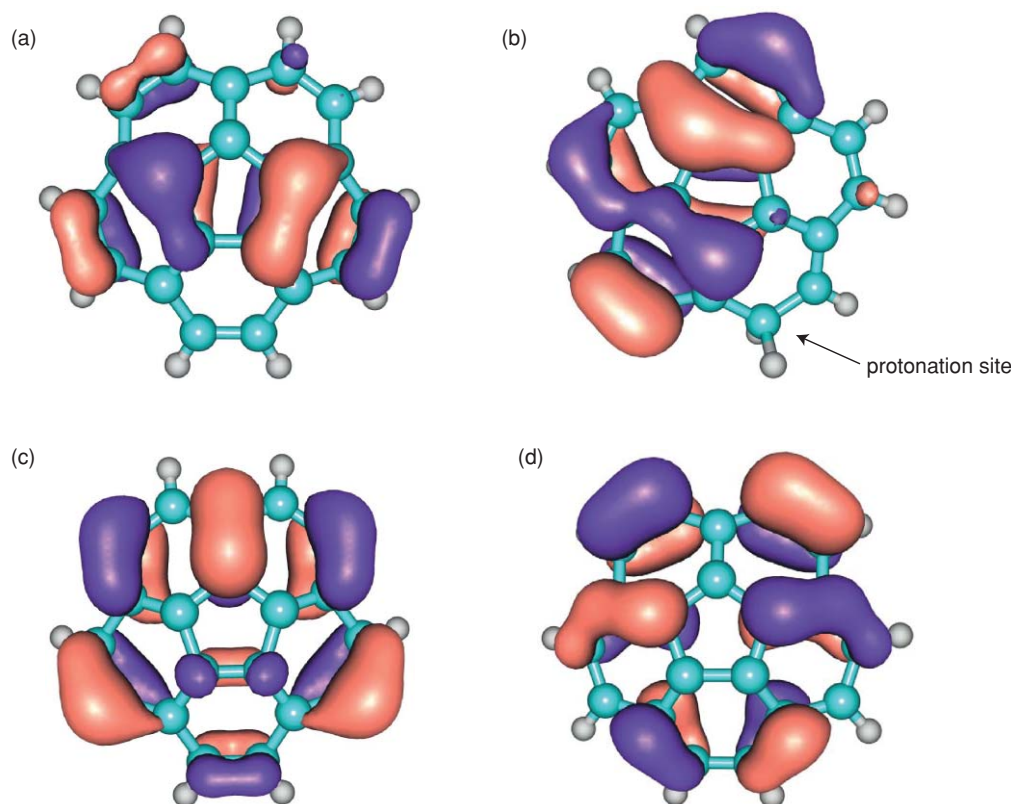


FIG. 1. The electron density isosurfaces of (a) the averaged twofold  $e_1$ -degenerate HOMO of neutral corannulene, (b) the HOMO of protonated corannulene, the SOMO of the cationic, (c) elongated ( $A'$ ) structure, and (d) compressed ( $A''$ ) structure.

Calculated energies and frequencies reported throughout this work are obtained using the B3LYP functional with the 6-311G(d,p) basis set unless noted otherwise.

### III. RESULTS

#### A. Electronic and geometric structures

Detailed structural parameters are listed in Table I (and in the inset of Fig. 2). For neutral corannulene, the HOMO electron density on the C atoms of the inner pentagonal ring is larger than in any other region of the molecule.<sup>29</sup> This is evident from the electron density isosurface of the HOMO shown in Fig. 1. Therefore, upon ionization (or protonation), changes in CC bond lengths are more significant in the inner ring than in any other part of the molecule, resulting in a very distinct change in the geometry of the pentagonal ring. Thus, the CC bond lengths of the pentagonal ring characterize the most important structural features of the three systems investigated. For neutral corannulene with  $C_{5v}$  symmetry, the pentagonal ring evidently has equal sides and hence the five optimized CC bond lengths ( $X_1, \dots, X_5$ ) are equivalent.

As detailed further in Sec. IV B, the JT vibronic interaction in the radical cation gives rise to one compressed and one elongated JT-distorted structure both of  $C_s$  symmetry. In this case, the  $C_s$  pentagon can be fully described by three of the five CC bond lengths ( $X_1, X_2$ , and  $X_3$ ). The structure will be called “compressed” if  $X_1 > X_3 > X_2$  (see Fig. 2), while the elongated structure refers to the situation where  $X_2 > X_3 > X_1$ . For the  $C_1$  geometry of protonated corannulene, all five sides

of the pentagonal ring are different and all CC bond lengths are required to describe the structure.

#### B. IR spectra

The IRMPD spectra of radical cation and protonated corannulene (corannulene<sup>+</sup> and corannuleneH<sup>+</sup>, respectively) are shown in Fig. 2. As described in Sec. II A, both spectra are recorded in the gas phase and differ essentially in the method of ionization (193-nm UV photoionization for the radical cation and ESI for the protonated species). Furthermore, in the ion trap experiment, the IR beam is focused more sharply than in the FTICR-MS setup. This is necessary because dissociation threshold of corannulene<sup>+</sup> is substantially higher than that of corannuleneH<sup>+</sup>: neutral  $C_{2n}H_x$  loss is observed for corannulene<sup>+</sup>, while the only decay channel observed for corannuleneH<sup>+</sup> is loss of atomic hydrogen, forming the radical cation (as was also observed for many protonated PAH molecules<sup>20</sup>). Dissociation of the radical cation involves unknown rearrangements, whereas in the protonated form, H-atom loss proceeds via a barrierless abstraction reaction, for which the activation energy is computed as 276 kJ/mol. The peak positions of the measured IRMPD bands are 835, 1092, 1154, 1222, 1332, and 1663  $\text{cm}^{-1}$  for corannulene<sup>+</sup>, and 850, 1198, 1320, 1394, and 1594  $\text{cm}^{-1}$  for corannuleneH<sup>+</sup>.

The FT-IR spectrum of neutral corannulene recorded in a KBr pellet is shown in the top panel of Fig. 2 for comparison. This spectrum was measured in order to validate

TABLE I. Ground-state energies and structural parameters of corannulene (neutral and radical cation) calculated at several *ab initio* and DFT levels. For the cation, energy values in boldface indicate the lower of the two states. The columns “*im*” list the values for the imaginary frequency (first-order saddle point) or “0” for true minima.

|       | $2A''$               |              |              |       |       |             | $2A'$                    |               |              |       |       |              | $(2A''-2A')$                   |              |        |        | $^1A_1$ (neutral) |                       |
|-------|----------------------|--------------|--------------|-------|-------|-------------|--------------------------|---------------|--------------|-------|-------|--------------|--------------------------------|--------------|--------|--------|-------------------|-----------------------|
|       | E                    |              | $\text{\AA}$ |       |       |             | $im$<br>$\text{cm}^{-1}$ | E<br>Hartrees | $\text{\AA}$ |       |       |              | $\Delta E$<br>$\text{cm}^{-1}$ | $\text{\AA}$ |        |        | E<br>Hartrees     | $X_o$<br>$\text{\AA}$ |
|       | $X_1$                | $X_2$        | $X_3$        | $X_1$ | $X_2$ | $X_3$       |                          |               | $X_1$        | $X_2$ | $X_3$ |              |                                |              |        |        |                   |                       |
| ROHF  | 6-31G                | -762.652 775 | 1.372        | 1.429 | 1.408 | 0           | 0                        | -762.651 834  | 1.427        | 1.397 | 1.417 | 729 <i>i</i> | -206                           | -0.055       | 0.032  | -0.009 |                   |                       |
|       | 6-31G( <i>d</i> )    | -762.930 625 | 1.371        | 1.428 | 1.409 | -           | -                        | -762.929 615  | 1.426        | 1.399 | 1.415 | 607 <i>i</i> | -222                           | -0.055       | 0.029  | -0.006 |                   |                       |
|       | 6-311G( <i>d,p</i> ) | -763.067 471 | 1.370        | 1.427 | 1.408 | -           | -                        | -763.066 510  | 1.426        | 1.398 | 1.415 | 570 <i>i</i> | -211                           | -0.056       | 0.029  | -0.007 |                   |                       |
|       | cc-pVDZ              | -762.980 222 | 1.373        | 1.430 | 1.411 | -           | -                        | -762.979 272  | 1.428        | 1.401 | 1.418 | 585 <i>i</i> | -209                           | -0.055       | 0.029  | -0.007 |                   |                       |
| BP86  | 6-31G                | -767.714 541 | 1.457        | 1.407 | 1.438 | 0           | 0                        | -767.714 556  | 1.401        | 1.452 | 1.420 | 22 <i>i</i>  | 3.3                            | 0.056        | -0.045 | 0.018  |                   |                       |
|       | 6-31G( <i>d</i> )    | -768.014 836 | 1.451        | 1.400 | 1.432 | 19 <i>i</i> | 19 <i>i</i>              | -768.014 863  | 1.395        | 1.446 | 1.414 | 0            | 6.0                            | 0.056        | -0.046 | 0.018  |                   |                       |
|       | 6-311G( <i>d,p</i> ) | -768.031 447 | 1.451        | 1.400 | 1.432 | 19 <i>i</i> | 19 <i>i</i>              | -768.031 473  | 1.395        | 1.446 | 1.414 | 0            | 5.8                            | 0.056        | -0.046 | 0.018  | -768.31100 1.422  |                       |
|       | cc-pVDZ              | -767.921 222 | 1.454        | 1.405 | 1.435 | 17 <i>i</i> | 17 <i>i</i>              | -767.921 244  | 1.399        | 1.449 | 1.418 | 0            | 4.8                            | 0.055        | -0.044 | 0.017  | -768.19763 1.425  |                       |
| BLYP  | 6-31G                | -767.402 926 | 1.461        | 1.409 | 1.440 | 0           | 0                        | -767.402 934  | 1.403        | 1.455 | 1.423 | 16 <i>i</i>  | 1.7                            | 0.058        | -0.046 | 0.017  |                   |                       |
|       | cc-pVDZ              | -767.605 064 | 1.458        | 1.407 | 1.438 | 2 <i>i</i>  | 2 <i>i</i>               | -767.605 078  | 1.402        | 1.453 | 1.421 | 0            | 3.2                            | 0.056        | -0.046 | 0.017  |                   |                       |
|       | 6-31G                | -767.695 356 | 1.450        | 1.396 | 1.432 | 0           | 0                        | -767.695 365  | 1.390        | 1.445 | 1.413 | 31 <i>i</i>  | 1.9                            | 0.060        | -0.049 | 0.019  |                   |                       |
|       | 6-31G( <i>d</i> )    | -767.878 220 | 1.446        | 1.393 | 1.427 | 0           | 0                        | -767.878 231  | 1.386        | 1.441 | 1.409 | 21 <i>i</i>  | 2.4                            | 0.060        | -0.048 | 0.018  |                   |                       |
| B3LYP | 6-311G( <i>d,p</i> ) | -768.034 631 | 1.445        | 1.391 | 1.426 | 0           | 0                        | -768.034 652  | 1.384        | 1.440 | 1.408 | 0            | 4.6                            | 0.061        | -0.049 | 0.018  | -768.31509 1.416  |                       |
|       | cc-pVDZ              | -767.917 605 | 1.448        | 1.396 | 1.430 | 0           | 0                        | -767.917 621  | 1.389        | 1.443 | 1.412 | 15 <i>i</i>  | 3.6                            | 0.059        | -0.047 | 0.018  | -768.19501 1.419  |                       |
|       | 6-31G                | -770.021 570 | 1.446        | 1.393 | 1.427 | 0           | 0                        | -770.021 588  | 1.387        | 1.441 | 1.409 | 20 <i>i</i>  | 3.9                            | 0.059        | -0.048 | 0.018  |                   |                       |
|       | 6-311G( <i>d</i> )   | -770.332 181 | 1.440        | 1.388 | 1.422 | 5 <i>i</i>  | 5 <i>i</i>               | -770.332 212  | 1.381        | 1.435 | 1.404 | 7 <i>i</i>   | 6.9                            | 0.059        | -0.047 | 0.018  |                   |                       |
| B3P86 | 6-311G( <i>d,p</i> ) | -770.349 143 | 1.440        | 1.388 | 1.422 | 6 <i>i</i>  | 6 <i>i</i>               | -770.349 174  | 1.381        | 1.435 | 1.404 | 10 <i>i</i>  | 6.8                            | 0.059        | -0.047 | 0.018  | -770.65370 1.411  |                       |
|       | cc-pVDZ              | -770.246 980 | 1.443        | 1.392 | 1.425 | 0           | 0                        | -770.247 006  | 1.385        | 1.438 | 1.408 | 0            | 5.8                            | 0.058        | -0.046 | 0.017  |                   |                       |



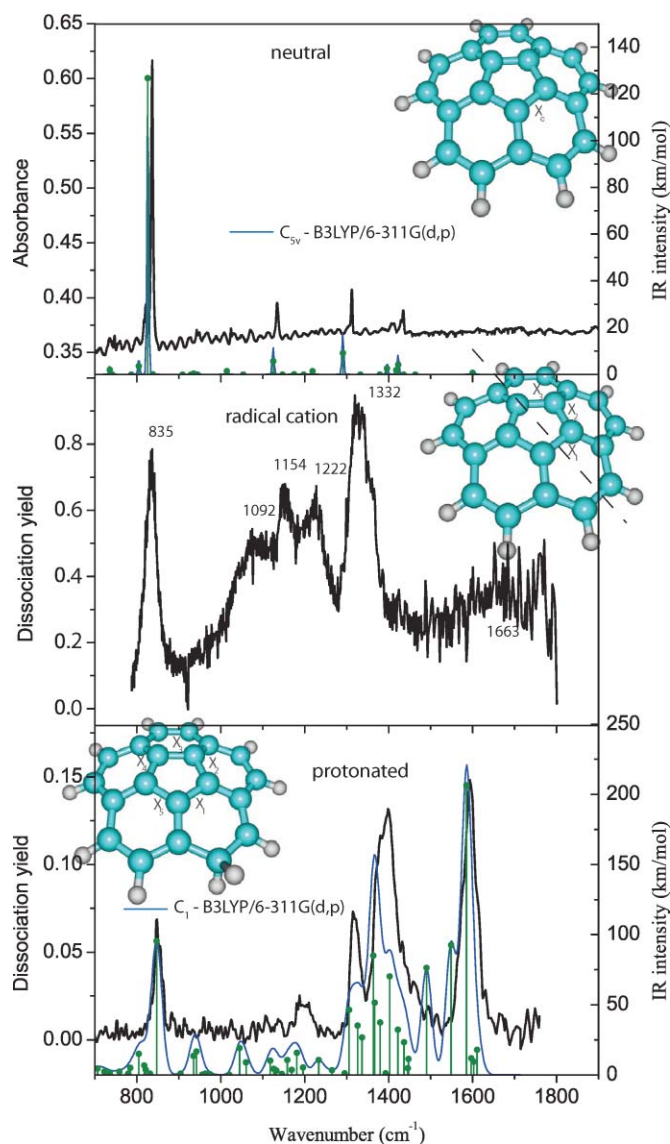


FIG. 2. FTIR KBr-pellet spectrum of neutral corannulene (top), and IRMPD spectra of corannulene<sup>+</sup> (middle) and corannuleneH<sup>+</sup> (bottom). Scaled harmonic B3LYP spectra are shown for neutral and protonated corannulene in green. The CC bond lengths of the pentagonal ring ( $X_i$ ) shown in the corannulene structures adopt five different values for the protonated system ( $C_1$  symmetry), three different values for the radical cation ( $C_s$  symmetry) and all values are equivalent for neutral corannulene ( $C_{5v}$  symmetry). Refer to text for further explanation.

the sample, and test the predictability and performance of selected theoretical methods on the corannulene system. Good agreement was found between this FT-IR spectrum and a previously recorded spectrum of neutral corannulene.<sup>30</sup>

Simulated IR spectra are generated using BP86 and B3LYP methods. Figure 2 compares the experimental spectra of the neutral and protonated corannulene with the B3LYP calculated spectrum, where the frequencies have been scaled by 0.9679.<sup>31</sup> In addition, the performance of the BP86 method was tested and a comparison is shown in Fig. S1 of the supplementary information.<sup>32</sup> Both methods show good agreement with FT-IR (neutral) and IRMPD (protonated) spectra. Contrary to the B3LYP harmonic calculation, where a scale factor is necessary in order to match the observed IRMPD

bands, the good agreement of unscaled BP86 harmonic bands with IRMPD bands is due to a partial compensation of underestimated harmonic frequencies and ignored vibrational anharmonicity, which is known to be particularly fortunate for this method.<sup>33</sup> A systematic analysis of the IR spectrum of corannulene<sup>+</sup> based on DFT calculations is presented in Sec. IV.

## IV. DISCUSSION

### A. Singlet systems: Neutral and protonated corannulene

There are  $3N-6 = 84$  vibrational degrees of freedom in corannulene spanning the linear combination of irreducible representations  $\Gamma_{\text{vib}} = 9A_1 + 7A_2 + 16E_1 + 18E_2$  in the  $C_{5v}$  point group. Symmetry-derived selection rules determine that modes of  $A_1$  and  $E_1$  species are the IR-active molecular vibrations in neutral corannulene. The totally symmetric CH “out-of-plane”  $a_1$ -mode at approximately  $840 \text{ cm}^{-1}$  is the most intense ( $127 \text{ km mol}^{-1}$ ), as observed in the FTIR spectrum and reproduced by the DFT calculation (Fig. 2, top).

Similar to regular polyaromatic hydrocarbon molecules,<sup>12,20,35,36</sup> corannulene protonates on one of the peripheral carbon atoms, forming a tetrahedral,  $sp^3$  hybridized site. Upon protonation, corannulene loses its symmetry completely and the extra H atom adds three new vibrational degrees of freedom. The (closed shell) singlet electronic state is preserved, though the electron density in the HOMO (predominantly localized at the center of the molecule in the neutral system) is now redistributed away from the ring bearing the extra H atom (see Fig. 1). This electronic configuration results in a well-defined  $C_1$  symmetry global minimum structure lying  $721 \text{ kJ/mol}$  lower in energy than the  $C_{5v}$ -minimum of neutral corannulene. The low symmetry structure is, for instance, revealed by the five nonequivalent CC bond lengths ( $X_1, \dots, X_5$ ) of the inner pentagonal ring. As will be further discussed below, this situation is very different from that of the radical cation, where removal of an electron from the degenerate  $e_1$ -HOMO of the neutral results in two  $C_s$ -symmetry PESs, which retain an intricate vibronic connection to the neutral  $C_{5v}$ -PES.

Charge redistribution in corannuleneH<sup>+</sup> induces substantial asymmetric carbon displacements enhancing the IR intensities of the CC stretching modes, observed in the IRMPD spectrum as two intense bands at  $1394$  and  $1594 \text{ cm}^{-1}$  (Fig. 2, bottom). Contrary to the cationic structure, where CH “in-plane” bends are predicted to couple strongly to CC stretches (in particular to those involving the five inner carbons), protonation tends to decouple CH in-plane bends from CC stretches. As a result, in the  $1000\text{--}1250 \text{ cm}^{-1}$  region of the experimental IRMPD spectra, the modes in corannuleneH<sup>+</sup> have much lower intensities than in corannulene<sup>+</sup>. In general, modes involving a multiple vibrational character are known to feature strong IR intensities in PAHs.<sup>37</sup>

The strong CH out-of-plane bending  $a_1$ -mode in the neutral system is considerably influenced by protonation and is found in the corannuleneH<sup>+</sup> IRMPD spectrum at  $850 \text{ cm}^{-1}$  with a slightly lower intensity, which at the

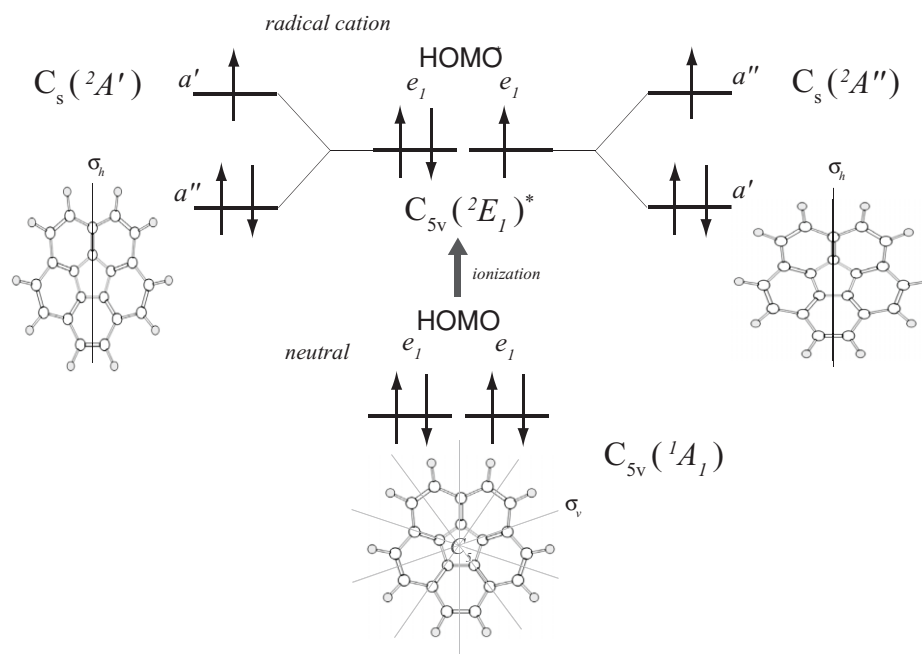


FIG. 3. The  $C_{5v}$  molecular structure of neutral corannulene at the bottom shows the  $C_5$  symmetry axis and the five equivalent mirror plane elements ( $\sigma_v$ ). The  $e_1$  twofold degenerate HOMO is illustrated and the totally symmetric representation of the  $C_{5v}$  point group is the ground electronic state of corannulene termed as  $^1A_1$ . Upon ionization, the resulting  $^2E_1$ -ground state of the open-shell corannulene cation is Jahn–Teller active and vibronic interaction (via  $E_2$  vibrational modes) lifts the degeneracy leading to two JT distorted  $C_s$  structures  $^2A'$  and  $^2A''$ , corresponding to elongated and compressed molecular geometries of the corannulene radical cation, respectively. The geometric distortion due the JT effect is exaggerated for illustration.

B3LYP/6-311G(d,p) level of theory amounts to  $95 \text{ km mol}^{-1}$ . The experimental spectra in Fig. 2 indeed clearly show the lowest relative CH out-of-plane intensity for the protonated system. As opposed to the neutral and radical, only eight local CH oscillators participate in this normal mode. The CH in-plane bending mode near  $1320 \text{ cm}^{-1}$  in the IRMPD spectrum, which is better reproduced at the BP86/6-311G(d,p) level of theory (Fig. S1 of supplementary information), has a strong local H–C–H scissoring character at the protonated site.

The general features in the spectrum of corannulene $H^+$ , that is, an isolated band assigned to a strong CH out-of-plane mode located near  $750 \text{ cm}^{-1}$ , the  $1200\text{--}1450 \text{ cm}^{-1}$  region featuring medium to strong intensity modes of somewhat mixed CH bending/CC stretching character, and a force constant enhancement in the CC stretching modes (as compared to unprotonated PAHs) yielding a band around  $1600 \text{ cm}^{-1}$ , have also been observed in previously measured IR spectra of protonated PAHs,<sup>20,36</sup> as well as in various protonated PAH derivatives.<sup>11,12,38</sup> The similarity in IR spectral features among the various protonated PAH species suggests that, in general, PAH IR spectra are primarily determined by the charge state and the closed- versus open-shell nature of the PAH.

## B. Doublet system: Corannulene radical cation

### 1. Jahn–Teller distorted structures

Neutral corannulene with  $C_{5v}$  symmetry has a twofold degenerate HOMO of  $E_1$  symmetry. Upon ionization,

removal of an electron lifts the degeneracy of the two  $e_1$  orbitals and according to the JT theorem,<sup>14</sup> vibrations of certain symmetry split the degenerate  $^2E_1$  state into symmetric and antisymmetric states of  $C_s$  symmetry.<sup>39</sup> The  $C_{5v}$  geometric structure distorts with respect to a mirror plane ( $\sigma_h$ ) resulting in a compressed and an elongated JT geometry of  $A''$  and  $A'$  symmetry. Figure 3 illustrates the closed-shell HOMO of the neutral system and the two possible (open-shell) singly occupied molecular orbitals (SOMO), which determine the molecular geometry and symmetry of each of the doublet states for the radical cation. The species of a nontotally symmetric vibration, appearing in the symmetry product of the two  $e_1$ -degenerate electronic wavefunctions, determine the type of molecular vibrations capable of lifting the degeneracy. For the  $C_{5v}$  point group, the direct product  $E_1 \times E_1$  contains the symmetry species  $A_1$ ,  $A_2$ , and  $E_2$ ,<sup>39</sup> and given that  $A_1$  and  $A_2$  retain the  $C_5$  axis, the modes with  $E_2$  symmetry are responsible for inducing the JT orbital adjustment. Although the nature of the JT interaction in the corannulene $^+$  system has not been experimentally investigated, it is understood from group theory that vibronic mixing of  $E_1$  (electronic) and  $E_2$  (vibration) species gives rise to the first order couplings,<sup>39,40</sup> and the interaction strengths have been previously calculated.<sup>29</sup>

Key structural parameters of the two JT-distorted geometries of corannulene $^+$  are listed in Table I. The lowest energy structure, for which values are shown in boldface, was found by all methods to be the elongated geometry (since  $X_2 > X_3 > X_1$ ). The *ab initio* ROHF assigns it to the  $^2A''$  electronic state, whereas all DFT methods assign it to the  $^2A'$  state.

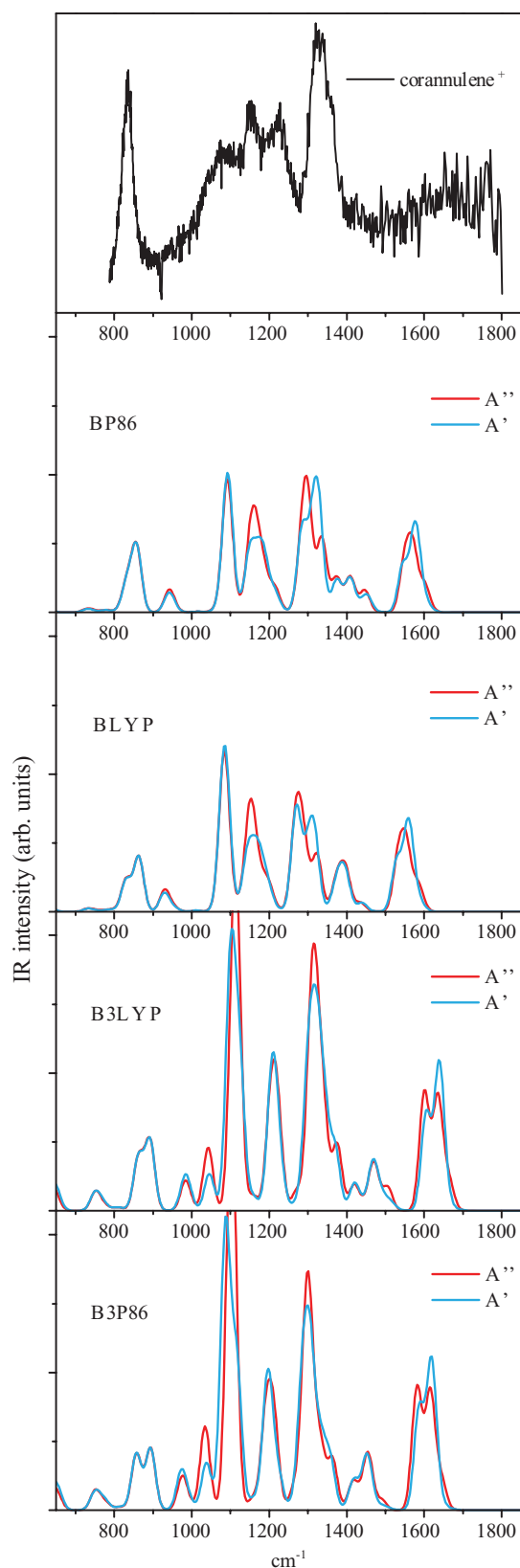


FIG. 4. IRMPD spectrum of corannulene<sup>+</sup> compared to harmonic IR spectra calculated with the BP86, BLYP, B3LYP, and B3P86 DFT methods employing the cc-pVDZ basis set.

However, the frequency calculations are not always consistent with the assignment of the minimum and saddle-point structures, which is probably a consequence of the small curvature of the potential.

For the lowest energy structure found at a particular level of computation, the Hessian matrix is positive definite (i.e., all frequencies are real) for the ROHF frequency computations, although those employing polarization functions failed to converge. For DFT methods, the Hessian has in some cases (depending on functional and basis set) one imaginary frequency indicating a local maximum in the direction of the relevant normal coordinate (saddle point). For any given DFT method, polarization functions have a strong impact on the assignment of the local minimum. For instance, employing the 6-31G basis set, the BP86 functional yields a small imaginary frequency for the lowest energy  $^2A'$  structure. In contrast, including polarization functions yields positive definite Hessians for the  $^2A'$  electronic structures and assigns the saddle point to the  $^2A''$  structures. The same behavior is found for BLYP. For hybrid functionals, the effect is somewhat less obvious. For instance, the B3LYP/6-311G(d,p) calculation yields positive definite Hessians for both  $^2A''$  and  $^2A'$  structures. This is reversed when the same 6-311G(d,p) basis set is used with B3P86, where two very small imaginary frequencies are found for both states. Then, using the latter method with the cc-pVDZ basis set yields the opposite result: all computed frequencies are real in both states.

The CC bond-length differences of the pentagonal ring between  $^2A''$  and  $^2A'$  structures are consistent among all calculations. Considering the reference  $C_{5v}$  neutral structure, the  $X_1$  and  $X_3$  CC bond lengths become shorter in the  $^2A'$  structure since the associated SOMO that results from removing an electron has an antibonding character for those two bonds, and  $X_2$  is longer as the SOMO is bonding.<sup>29,41</sup> Conversely for  $^2A''$ , the  $X_1$  and  $X_3$  CC bond lengths become longer and  $X_2$  CC bond length shorter, given that the SOMO is bonding for  $X_1$  and  $X_3$ , and antibonding for  $X_2$ . For DFT methods, the average differences for CC bond lengths are 0.058 ( $\Delta X_1$ ),  $-0.047$  ( $\Delta X_2$ ), and 0.018 ( $\Delta X_3$ ) Å (see Table I).

Because there are five equivalent mirror planes in corannulene (see Fig. 3), the radical cation features five equivalent minima of  $C_s$  symmetry located in a circular “moat” around the symmetric  $C_{5v}$  JT conical intersection. For the corannulene radical anion, a barrier between the five equivalent minima of about  $18\text{ cm}^{-1}$  was experimentally determined via ESR spectroscopy.<sup>42</sup> This was interpreted as the anion transiting ten stationary  $C_s$  points (five minima and five saddle points) along the PES moat. In the cation, the  $^2A''$  and  $^2A'$  structures were found to be very close in energy for all DFT levels, which explains the inconsistencies in assigning either of the states as the minimum energy structure. The largest energy difference found at the B3P86/6-31G(d) level is  $6.9\text{ cm}^{-1}$ , while the smallest is only  $1.7\text{ cm}^{-1}$  at the BLYP/6-31G level. An average difference of  $5.7\text{ cm}^{-1}$  is obtained for the 6-311G(d,p) basis-set calculations, which gives us a notion of the tiny barrier between the minima in the PES moat. Although the energy barrier computed here is perhaps not accurate, the so-called *pseudorotation* in the anion is expected in the corannulene radical cation as well, resulting in a dynamical JT distorted system.



## 2. Vibrational structure and IRMPD spectrum

The IRMPD spectrum of the corannulene radical cation, shown in the top panel of Fig. 4, features a number of clearly recognizable, though fairly broad resonances. As compared to the experiment on protonated corannulene, we note that in this case an oven was used to evaporate the sample and that the dissociation threshold of the radical cation is substantially higher than that of the protonated species. The observed bandwidths are primarily a consequence of the IRMPD excitation mechanism, which involves anharmonic shifting and broadening effects increasing with internal energy,<sup>43</sup> in combination with the rotational envelope and the appearance of hot bands at the temperature of the oven (353 K). Due to the high internal energy contained in the corannulene ions, anharmonic couplings between various vibrational modes likely further influence the band shapes observed.<sup>44</sup> At 353 K, the number of vibrational combination levels per  $\text{cm}^{-1}$  is on the order of  $10^6$  as estimated from the harmonic frequencies and a direct count using the Beyer–Swinehart algorithm.<sup>45</sup> The average internal energy per corannulene ion is then around  $3140 \text{ cm}^{-1}$ .

Figure 4 as well as Figs. S2–S5 in the supplementary information compare the experimental IRMPD spectrum with spectra calculated at various DFT levels. For a more consistent comparison, no scaling of the harmonic frequencies has been applied.

In a previous study on the JT vibronic couplings in corannulene<sup>+</sup>, it was found that three out of the 18 JT-active  $E_2$  modes in the reference  $C_{5v}$  neutral structure, with computed values of 439, 648, and  $1498 \text{ cm}^{-1}$  at the B3LYP/6-31G(d) level, exhibit the strongest linear vibronic coupling to the  $e_1$ -HOMO.<sup>29</sup> Using the 6-311G(d,p) basis set with same DFT method, these modes are located at 440, 650, and  $1484 \text{ cm}^{-1}$ , respectively. Animation of these modes reveals that they are characterized by having large carbon displacements, as indicated by their computed reduced masses of 7.9, 6.5, and  $7.5 \text{ amu}$ , respectively. Overall, they involve a substantial deformation of the pentagonal inner ring, where the HOMO electron density is largely localized, thus explaining their strong coupling through significant orbital interactions among neighboring pentagonal carbons.<sup>29</sup>

As shown in Fig. 1 of Ref. 29 and corroborated by the present calculations, the vibrational patterns of the three vibronic JT-active  $E_2$  modes clearly induce nuclear displacements in the direction of the structural change from the  $C_{5v}$  neutral corannulene structure to the cationic  $C_s$  structure(s). In general,  $E_2$  modes contain elements of mirror plane symmetry as recognized from the symmetry-descending correlation between  $C_{5v}$  and its subgroup  $C_s$ , that is, the  $E_2$  representation converts as  $E_2 \rightarrow A' + A''$ .<sup>46</sup> Therefore, the substantial atomic orbital mixing among pentagonal carbons in the direction of the three JT-active  $E_2$  modes generates stationary structures having compressed ( $A''$ ) or elongated ( $A'$ ) geometries.

The harmonic vibrational frequencies calculated for both  ${}^2A'$  and  ${}^2A''$  structures are mostly similar, and as a result, the simulated  $30 \text{ cm}^{-1}$  FWHM IR spectra (Figs. 4 and S2–S5) of the two states are almost indistinguishable at any particular DFT level. The only variations seen are essentially

in relative intensities. For instance, in the pure DFT methods (BP86 and BLYP) the largest intensity variation is found for the band with CH in-plane bending character computed roughly at  $1170 \text{ cm}^{-1}$  (Figs. S2 and S3). The intensity of this band is larger in the  ${}^2A''$  state by about 50% (except for the 6-31G basis set calculations where it is about 90% larger). For hybrid-DFT methods (B3LYP and B3P86; see Figs. S4 and S5), the largest intensity variation is seen in the band at roughly  $1100 \text{ cm}^{-1}$  (this band is predicted at  $\sim 1090 \text{ cm}^{-1}$  for BP86 and BLYP methods). For instance, in the cc-pVDZ basis-set calculations (see Fig. 4), its intensity in the  ${}^2A''$  state is 30% larger for both hybrid functionals. We note that this band also has CH bending character. Other bands in the spectrum appear nearly equal. For each particular DFT method, the main effect of a higher basis set is a correction of the relative intensity of the band at  $1100 \text{ cm}^{-1}$  (or at  $1090 \text{ cm}^{-1}$  for pure DFT methods), which is similar for both electronic states. This effect increasingly favors the match with the experimental IRMPD spectrum. At the highest levels of theory used, that is, those combining hybrid functionals with 6-311G(d,p) and cc-pVDZ basis sets, the calculated spectra are virtually identical. As the cc-pVDZ harmonic calculations reproduce the observed relative intensities slightly better (see Fig. S2), in particular, for the observed  $1222 \text{ cm}^{-1}$  band, these calculations are used for the spectral comparisons in Fig. 4.

It is observed that all intensity variations found among DFT levels involve the CH bending modes in the  $1000$ – $1250 \text{ cm}^{-1}$  region. In the IRMPD spectrum, three close-lying semiresolved bands at approximately 1092, 1154, and  $1222 \text{ cm}^{-1}$  dominate this region. Inspection of the four DFT spectra calculated with the cc-pVDZ basis set (see Fig. 4) reveals that there are also three bands with predicted peak positions close to the three experimental bands, although the intensity pattern is clearly different. As already stated, these bands are characterized by symmetric ( $A'$ ) and antisymmetric ( $A''$ ) CH in-plane bending vibrations, although they also involve substantial in-plane stretching displacements of the five central carbons.

The weakest of the three bands, seen in hybrid B3P86 and B3LYP spectra near  $1040 \text{ cm}^{-1}$ , is unnoticeable to the eye in pure BP86 and BLYP spectra. This band, due to a single  $a'$ -mode, involves a strong CC-stretching character of the pentagonal inner ring. Along this mode, an induced change in electronic structure is expected, since it is known that in addition to  $\pi$ -orbital interactions among the five central carbons,  $\sigma$ -orbital interactions occur due to the curved geometry of corannulene; this contrasts planar PAH structures such as coronene, where orbital interactions are exclusively between  $\pi$  orbitals of neighboring carbons.<sup>2,29</sup> The discrepancy in intensities as predicted by pure and hybrid functionals is possibly related to the different SOMO density distributions calculated by these methods, as it has been suggested that the phase patterns of these distributions influence the IR mode intensities.<sup>37,41,47</sup> Furthermore, animation of the  $1040 \text{ cm}^{-1}$  mode shows that it deforms the cation alternately between compressed and elongated geometries of the JT distorted cation, which possibly relates to the vibronic interaction in corannulene<sup>+</sup>. Its peak position calculated

with the hybrid functionals, although somewhat redshifted, closely approximates the relatively broad band in the IRMPD spectrum centered at  $1092\text{ cm}^{-1}$ . Thus, the  $1092$ ,  $1154$ , and  $1222\text{ cm}^{-1}$  IRMPD bands are tentatively assigned to the nominal  $1040$ ,  $1100$ , and  $1200\text{ cm}^{-1}$  bands as calculated by the highest-level hybrid-DFT methods employed here (B3LYP and B3P86 spectra in Fig. 4).

The IRMPD bands at  $835$  and  $1332\text{ cm}^{-1}$  appear well resolved in the IRMPD spectrum, and present a FWHM of  $25$  and  $52\text{ cm}^{-1}$ , respectively. The intensity of the  $835\text{ cm}^{-1}$  IRMPD band is, according to theory, chiefly carried by a single symmetric CH out-of-plane bending mode and to a lesser extent, by two neighboring  $a'$  and  $a''$  modes of similar intensity characterized as breathing deformations of the five benzenoid rings. The narrow profile seen in the experiment is best reproduced at the BP86/cc-pVDZ level. In the hybrid-DFT spectra a splitting of this band is predicted owing to the neighboring  $a'$  and  $a''$  modes, which are computed at slightly lower frequencies. The  $1332\text{ cm}^{-1}$  IRMPD band is reproduced by the nominal  $1300\text{ cm}^{-1}$  hybrid-DFT harmonic band, and therefore assigned to an admixture of CH in-plane bending and CC stretching modes. Based on the harmonic band nominally located at  $1630\text{ cm}^{-1}$  in the hybrid functional spectra (or at  $1580\text{ cm}^{-1}$  for the BLYP and BP86 functionals), the very broad IRMPD signal centered around  $1663\text{ cm}^{-1}$  is assigned as being due to CC stretching modes, where the carbons of the pentagonal ring display the largest displacements. Possibly, large anharmonicities of these modes cause the extreme broadening observed in the IRMPD spectrum. The increase in signal around  $1760\text{ cm}^{-1}$  is an artifact that results from the decreasing FELIX power in this range in combination with the linear power-correction applied.

In summary, the calculated spectra give a qualitative match to the experimental spectrum, where the hybrid functionals appear to be slightly better than the pure functionals. The vibrational character of the modes calculated for the corannulene radical cation is consistent with the character of the modes found in other PAH cationic structures

investigated before. Nevertheless, all experimental bands are blueshifted compared to the calculated harmonic frequencies, even though no scaling was applied and even though IRMPD bands are typically redshifted compared to linear absorption spectra. In contrast, bands for the neutral and protonated systems were accurately predicted. This outcome further indicates that, contrary to the two singlet systems studied here, the doublet radical cation does not rest on a well-defined single PES, but instead, on an intricate  ${}^2A''$ - ${}^2A'$  PES with angular dependence around the JT  $C_{5v}$  conical intersection, as is the case for the corannulene anion.<sup>42</sup> In contrast to many cationic PAHs,<sup>10,11,16,48</sup> where it has been shown that their IRMPD spectra can be successfully analyzed with linear-absorption harmonic DFT spectra, a comprehensive understanding of the observed IRMPD spectrum of the corannulene radical cation requires a more rigorous theoretical approach, which is beyond the scope of this investigation.

### 3. Effects of nonplanarity in the PAH framework: Corannulene<sup>+</sup> versus coronene<sup>+</sup>

In Fig. 5 we compare the corannulene<sup>+</sup> IRMPD spectrum with the corresponding IRMPD spectrum of coronene<sup>+</sup>.<sup>49</sup> As anticipated, the largest distinction observed is an intensity enhancement of the CH in-plane bending modes around  $1000$ – $1250\text{ cm}^{-1}$ . This is a clear indication of the influence of the inner pentagonal ring in corannulene<sup>+</sup>, which undergoes pronounced deformations for vibrational modes in this frequency range. These likely induce charge redistributions that are not present in the higher-symmetry planar coronene<sup>+</sup>, and which are expected to have an effect on the dipole derivatives enhancing the IR activity of those modes.

In general, the strong IR intensities typical of PAH cations are the effect of long and short range charge fluxes among aromatic rings as a consequence of electron-vibration interactions.<sup>41,47</sup> Because of the pentagonal-ring deformations inherent to the warped structure, these charge fluctuations are stronger in corannulene<sup>+</sup> than in the planar coronene<sup>+</sup>. This explains why the computed linear vibronic couplings for corannulene<sup>+</sup> are larger than those computed for coronene<sup>+</sup>.<sup>29</sup>

An important implication is that the modes in the  $1000$ – $1250\text{ cm}^{-1}$  region featuring substantial intensity enhancement in corannulene<sup>+</sup> have a more mixed mode character<sup>37</sup> than in coronene<sup>+</sup>. Dynamic charge polarizations are, therefore, generally larger for corannulene<sup>+</sup> giving rise to larger dipole derivatives. Normal modes in this spectral range for corannulene<sup>+</sup> involve both CH in-plane bends and CC stretches (mainly within the pentagonal inner ring), while for coronene<sup>+</sup> they appear to have more pure CH in-plane character. Interestingly, planar PAH cations having a pentagonal ring also show an intensity enhancement of CH in-plane bending modes in the same spectral region<sup>48</sup> as compared to regular cationic PAHs of similar sizes.

The strong CH out-of-plane vibration near  $840\text{ cm}^{-1}$  is qualitatively similar in both cationic systems, showing up as a well-resolved band in the far-IR range of the IRMPD spectrum, although in corannulene<sup>+</sup> it appears to be somewhat more intense. The similar position for both species is expected

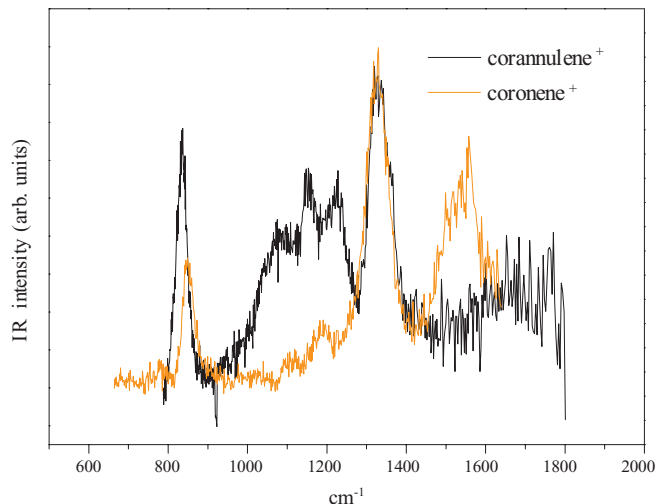


FIG. 5. Comparison of the IRMPD spectra of corannulene and coronene radical cations.

based on the fact that both have only doubly adjacent CH groups (or “duets”) on their periphery.<sup>50</sup> The admixture of CH bends and CC stretches, featured in both corannulene<sup>+</sup> and coronene<sup>+</sup> as an intense well-resolved IRMPD band at 1332 cm<sup>-1</sup> and 1330 cm<sup>-1</sup>, respectively, are virtually identical. To the high-frequency end of the spectral range studied, the IR activity observed in the corannulene<sup>+</sup> and coronene<sup>+</sup> spectra is carried by CC stretching modes. The nonplanar structure in corannulene<sup>+</sup> appears to induce larger force constants, which cause a blueshift of these modes with respect to those in coronene<sup>+</sup>.

## V. CONCLUSIONS

Infrared multiple-photon dissociation spectroscopy was applied to record the gas-phase spectra of protonated corannulene and the corannulene radical cation. Good agreement was found between the experimental IR spectrum of protonated corannulene and the computed spectrum for a structure where one of the peripheral C-atoms is protonated. The spectral features of protonated corannulene are analogous to those recently observed for various protonated PAH species. This similarity is believed to be due to the combined effect of charge ( $q = +1$ ) and spin ( $S = 0$ ) states common among the protonated PAHs.

The corannulene radical cation undergoes Jahn–Teller distortion as a consequence of the degenerate HOMO in the neutral molecule. Extensive DFT calculations were performed for the radical cation in its two distorted C<sub>s</sub> geometries. The computed energy difference between <sup>2</sup>A' and <sup>2</sup>A'' structures is small, thus suggesting a dynamical Jahn–Teller distortion of the corannulene radical cation. Accordingly, strictly speaking, its doublet ground state cannot be associated with a single optimized local-minimum structure. Therefore, while a comparison of the experimental IRMPD spectrum with harmonic DFT spectra gives a qualitative, overall agreement at the highest levels of theory employed, a one-to-one assignment of each of the bands remains speculative. Of all computational methods used, the best match was found for B3LYP and B3P86, employing both the cc-pVDZ and 6-311G(d,p) function sets.

A comparison between the IRMPD spectra of corannulene<sup>+</sup> and its “planar analog” coronene<sup>+</sup> shows the influence of charge redistribution on relative intensities along certain frequency modes. In particular, modes involving CC stretching vibrations within the pentagonal inner ring are largely affected. Especially in the 1000–1250 cm<sup>-1</sup> region, the IR intensities in corannulene<sup>+</sup> are substantially higher than in coronene<sup>+</sup>. Spectral comparison was also made with the positively charged corannuleneH<sup>+</sup>, where the extra hydrogen changes the structure and symmetry reducing the pentagonal CC stretching character in these modes. In coronene<sup>+</sup> and corannuleneH<sup>+</sup>, the modes are characterized mainly by CH in-plane bends, whereas in corannulene<sup>+</sup>, they involve both CH bends and CC stretches, chiefly among carbons of the highly vibronically active pentagonal ring.

## ACKNOWLEDGMENTS

The research leading to these results has received funding from the European Community's Seventh Framework Programme (FP7/2007-2013) under Grant Agreement No. 226716. Additionally, it was supported by the Swiss National Science Foundation (No. 200020-124349/1). We thank FOM for providing beam time, as well as the FELIX staff for their skillful technical support. The Siegel Group, especially A. Butterfield, is most graciously thanked for the sample preparation. J.O. gratefully acknowledges support by the Stichting Physica. This work is also part of the research program of FOM, which is financially supported by the Nederlandse Organisatie voor Wetenschappelijk Onderzoek (NWO).

- <sup>1</sup>J. C. Hanson and C. E. Nordman, *Acta Crystallogr., Sect. B: Struct. Crystallogr. Cryst. Chem.* **B32**, 1147 (1976).
- <sup>2</sup>T. Kato and T. Yamabe, *J. Chem. Phys.* **117**, 2324 (2002).
- <sup>3</sup>L. G. Scanlon, P. B. Balbuena, Y. Zhang, G. Sandi, C. K. Back, W. A. Feld, J. Mack, M. A. Rottmayer, and J. L. Riepenhoff, *J. Phys. Chem. B* **110**, 7688 (2006).
- <sup>4</sup>L. Kobryn, W. P. Henry, F. R. Fronczek, R. Sygula, and A. Sygula, *Tetrahedron Lett.* **50**, 7124 (2009).
- <sup>5</sup>D. A. García-Hernández, A. Manchado, P. García-Lario, L. Stanghellini, E. Villaver, R. A. Shaw, R. Szczerba, and J. V. Perea-Calderón, *Astrophys. J.* **724L** (2010); J. Cami, J. Bernard-Salas, E. Peeters, and S. E. Malek, *Science* **329** (2010); H. Kroto, *Angew. Chem., Int. Ed.* **36**, 1578 (1997); K. Sellgren, M. W. Werner, J. G. Ingalls, J. D. T. Smith, T. M. Carleton, and C. Joblin, *Astrophys. J.* **722**, L54 (2010).
- <sup>6</sup>K. K. Baldrige and J. S. Siegel, *Theor. Chem. Acc.* **97**, 67 (1997).
- <sup>7</sup>F. J. Lovas, R. J. McMahon, J.-U. Grabow, M. Schnell, J. Mack, L. T. Scott, and R. L. Kuczkowski, *J. Am. Chem. Soc.* **127**, 4345 (2005); P. Pilleri, D. Herberth, T. F. Giesen, M. Gerin, C. Joblin, G. Mulas, G. Mallocci, J. U. Grabow, S. Brünken, L. Surin, B. D. Steinberg, K. R. Curtis, and L. T. Scott, *Mon. Not. R. Astron. Soc.* **397**, 1053 (2009).
- <sup>8</sup>F. Pauzat, D. Talbi, and Y. Ellinger, *Astron. Astrophys.* **319**, 318 (1997); G. Mallocci, C. Joblin, and G. Mulas, *ibid.*, **462**, 627 (2007).
- <sup>9</sup>S. R. Langhoff, *J. Phys. Chem.* **100**, 2819 (1996).
- <sup>10</sup>J. Oomens, A. G. G. M. Tielens, B. G. Sartakov, G. von Helden, and G. Meijer, *Astrophys. J.* **591**, 968 (2003).
- <sup>11</sup>H. A. Galué, O. Pirali, and J. Oomens, *Astron. Astrophys.* **517**, A15 (2010).
- <sup>12</sup>D. Zhao, J. Langer, J. Oomens, and O. Dopfer, *J. Chem. Phys.* **131**, 184307 (2009).
- <sup>13</sup>C. W. Bauschlicher, D. M. Hudgins, and L. J. Allamandola, *Theor. Chem. Acc.* **103**, 154 (1999).
- <sup>14</sup>H. A. Jahn and E. Teller, *Proc. R. Soc. London, Ser. A* **161**, 220 (1937).
- <sup>15</sup>T. J. Seiders, E. L. Elliott, G. H. Grube, and J. S. Siegel, *J. Am. Chem. Soc.* **121**, 7804 (1999).
- <sup>16</sup>J. Oomens, A. J. A. van Roij, G. Meijer, and G. von Helden, *Astrophys. J.* **542**, 404 (2000).
- <sup>17</sup>S. Denifl, B. Sonnweber, J. Mack, L. T. Scott, P. Scheier, K. Becker, and T. D. Mark, *Int. J. Mass Spectrom.* **249-250**, 353 (2006).
- <sup>18</sup>D. Oepts, A. F. G. Van Der Meer, and P. W. van Amersfoort, *Infrared Phys. Technol.* **36**(1), 297 (1995).
- <sup>19</sup>N. C. Polfer and J. Oomens, *Phys. Chem. Chem. Phys.* **9**, 3804 (2007).
- <sup>20</sup>H. Knorke, J. Langer, J. Oomens, and O. Dopfer, *Astrophys. J.* **706**, L66 (2009).
- <sup>21</sup>C. C. J. Roothaan, *Rev. Mod. Phys.* **23**, 69 (1951).
- <sup>22</sup>J. S. Binkley, J. A. Pople, and P. A. Dobosh, *Mol. Phys.* **28**, 1423 (1974).
- <sup>23</sup>A. D. Becke, *Phys. Rev. A* **38**, 3098 (1988).
- <sup>24</sup>J. P. Perdew, *Phys. Rev. B* **33**, 8822 (1986).
- <sup>25</sup>C. Lee, W. Yang, and R. G. Parr, *Phys. Rev. B* **37**, 785 (1988).
- <sup>26</sup>A. D. Becke, *J. Chem. Phys.* **98**, 5648 (1993).
- <sup>27</sup>T. H. Dunning, *J. Chem. Phys.* **90**, 1007 (1989).
- <sup>28</sup>M. J. Frisch, G. W. Trucks, H. B. Schlegel *et al.*, GAUSSIAN 03, Revision C.02, Gaussian, Inc., Wallingford, CT, 2004.
- <sup>29</sup>T. Kato and T. Yamabe, *J. Phys. Chem. A* **110**, 2785 (2006).

- <sup>30</sup>G. Rouillé, C. Jäger, M. Steglich, F. Huisken, T. Henning, G. Theumer, I. Bauer, and H.-J. Knölker, *Chem. Phys. Chem.* **9**, 2085 (2008).
- <sup>31</sup>M. P. Andersson and P. Uvdal, *J. Phys. Chem.* **109**, 2937 (2005).
- <sup>32</sup>See supplementary material at <http://dx.doi.org/10.1063/1.3540661> for spectra calculated using different DFT methods.
- <sup>33</sup>J. Neugebauer and B. A. Hess, *J. Chem. Phys.* **118**, 7215 (2003).
- <sup>34</sup>We adopt the nomenclature that is usual for regular, planar PAH molecules.
- <sup>35</sup>D. M. Hudgins, C. W. Bauschlicher, and L. J. Allamandola, *Spectrochim. Acta, Part A* **57**, 907 (2001); L. J. Lorenz, N. Solca, J. Lemaire, P. Maitre, and O. Dopfer, *Angew. Chem., Int. Ed.* **46**, 6714 (2007).
- <sup>36</sup>A. M. Ricks, G. E. Douberly, and M. A. Duncan, *Astrophys. J.* **702**, 301 (2009).
- <sup>37</sup>H. Torii, *Vib. Spectrosc.* **24**, 3 (2000).
- <sup>38</sup>M. Vala, J. Szczepanski, J. Oomens, and J. Steill, *J. Am. Chem. Soc.* **131**, 5784 (2009).
- <sup>39</sup>G. Herzberg, *Molecular Spectra and Molecular Structure* (Krieger Publishing Company, Malabar, FL, 1945).
- <sup>40</sup>T. A. Barckholtz and T. A. Miller, *Int. Rev. Phys. Chem.* **17**, 435 (1998).
- <sup>41</sup>H. Torii, *Chem. Phys. Lett.* **306**, 381 (1999).
- <sup>42</sup>T. Sato, A. Yamamoto, and H. Tanaka, *Chem. Phys. Lett.* **326**, 573 (2000).
- <sup>43</sup>J. Oomens, B. G. Sartakov, G. Meijer, and G. v. Helden, *Int. J. Mass Spectrom.* **254**, 1 (2006).
- <sup>44</sup>D. A. Sadovskii and B. I. Zhilinskii, *J. Chem. Phys.* **103** (1995); M. E. Kellman and V. Tyng, *Acc. Chem. Res.* **40**, 243 (2007).
- <sup>45</sup>S. E. Stein and B. S. Rabinovitch, *J. Chem. Phys.* **58**, 2438 (1973).
- <sup>46</sup>J. E. Bright Wilson, J. C. Decius, and P. C. Cross, *Molecular Vibrations: The Theory of Infrared and Raman Vibrational Spectra* (Dover, New York, 1955).
- <sup>47</sup>H. Torii, Y. Ueno, A. Sakamoto, and M. Tasumi, *J. Phys. Chem. A* **103**, 5557 (1999).
- <sup>48</sup>J. Oomens, G. Meijer, and G. v. Helden, *J. Phys. Chem. A* **105**, 8302 (2001).
- <sup>49</sup>J. Oomens, B. G. Sartakov, A. G. G. M. Tielens, G. Meijer, and G. v. Helden, *Astrophys. J.* **560**, L99 (2001).
- <sup>50</sup>D. M. Hudgins and L. J. Allamandola, *Astrophys. J.* **516**, L41 (1999).